



<b>Title</b>	<b>Pinned modes in two-dimensional lossy lattices with local gain and nonlinearity</b>
<b>Author(s)</b>	<b>Ding, E; Tang, AYS; Chow, KW; Malomed, BA</b>
<b>Citation</b>	<b>Philosophical Transactions of the Royal Society A: Mathematical, Physical and Engineering Sciences, 2014, v. 372 n. 2027</b>
<b>Issued Date</b>	<b>2014</b>
<b>URL</b>	<b><a href="http://hdl.handle.net/10722/210743">http://hdl.handle.net/10722/210743</a></b>
<b>Rights</b>	<b>Creative Commons: Attribution 3.0 Hong Kong License</b>

# Pinned modes in two-dimensional lossy lattices with local gain and nonlinearity

A. Tang and K. W. Chow

*Department of Mechanical Engineering, University of Hong Kong, Pokfulam Road, Hong Kong*

Edwin Ding

*Department of Mathematics and Physics, Azusa Pacific University, Box 7000, Azusa, CA 91702-7000, USA*

Boris A. Malomed

*Department of Physical Electronics, School of Electrical Engineering,  
Faculty of Engineering, Tel Aviv University, Tel Aviv 69978, Israel*

## I. INTRODUCTION

The present work explores the generation of stable solitons in two-dimensional (2D) discrete waveguiding arrays (lattices) with a localized nonlinear gain. In particular, we demonstrate that this is possible in a linear lattice where the nonlinearity, represented by the self-phase modulation and cubic gain, is applied to a single waveguide (the hot spot, HS). The lattice coupled Ginzburg-Landau (CGL) system which is introduced here may be used for selective excitation of particular core(s) in an arrayed waveguiding system, if it is uniformly doped, but only the selected core is pumped by an external coherent source of light.

The paper is organized as follows. The discrete 2D CGL equation is introduced in Sec. II. Section III outlines an approximate analysis for the truncated version of the model. The linear stability analysis of the pinned solitons against small perturbations is presented in Sec. IV. Section V discusses about the onset of instability of the zero solution. A brief discussion of the double HS problem is given in Sec. VI, followed by a conclusion in Sec. VII.

## II. THE MODEL

The present work aims to consider the 2D counterpart of the lattice model introduced in Ref. [6]:

$$\frac{du_{m,n}}{dz} = \frac{i}{2} (u_{m-1,n} + u_{m+1,n} + u_{m,n-1} + u_{m,n+1} - 4u_{m,n}) - \gamma u_{m,n} + [(\Gamma_1 + i\Gamma_2) + (iB - E)|u_{m,n}|^2] \delta_{m,0} \delta_{n,0} u_{m,n}, \quad (1)$$

where  $m, n = 0, \pm 1, \pm 2, \dots$  are the discrete coordinate,  $\delta_{m,0}$  and  $\delta_{n,0}$  are the Kronecker's symbols, and the coefficient of the linear coupling between adjacent cores is scaled to unity. In optics, the discrete equation can be derived by means of well-known methods [1–3]. In the application to arrays of plasmonic waveguides, which can be built, for example, as a set of metallic nanowires mounted on top of a dielectric structure [4], this equation can be derived in the adiabatic approximation, when the exciton field may be eliminated in favor of the photonic component (otherwise, the system features a two-

component discrete structure). It is also relevant to mention that the well-known *staggering transformation* [3],  $u_{m,n}(t) \equiv (-1)^{m+n} e^{-4it} \tilde{u}_{m,n}^*$ , where the asterisk stands for the complex conjugate, simultaneously reverses the signs of  $\Gamma_2$  and  $B$ , thus rendering the self-focusing and defocusing nonlinearities mutually convertible in the discrete system. In particular, the latter feature is essential for modeling arrays of plasmonic waveguides, where the intrinsic excitonic nonlinearity is self-repulsive. In what follows, we fix the signs of  $\Gamma_2$  and  $B$  by setting  $\Gamma_2 > 0$ , while  $B$  may be positive (self-focusing), negative (self-defocusing), or zero.

As mentioned above, the underlying array can be actually manufactured as a uniform one, with all the cores doped by an appropriate amplifying material, while the HS is singled out by focusing an external pump to a single core. The latter setting is interesting for potential applications, as the location of the HS is switchable in the 2D plane.

The model based on Eq. (1) is the subject of the present paper. The Kerr-nonlinearity coefficient, if present, may be normalized to  $B = +1$  (self-focusing) or  $B = -1$  (self-defocusing). These two cases are considered separately below, along with the case of  $B = 0$ , when the nonlinearity is represented solely by the cubic dissipation localized at the HS.

## III. TRUNCATED LATTICE ANALYSIS

One-dimensional dissipative solitons in uniform discrete CGL equations were studied by means of numerical methods in Refs. [2, 5]. We seek analytical solutions for stationary modes with real propagation constant  $k$  as

$$u_{m,n}(z) = U_{m,n} e^{ikz}. \quad (2)$$

Outside of the HS site,  $m = n = 0$ , Eq. (1) gives rise to the linear stationary equation,

$$2(k + 2 - i\gamma) U_{m,n} = U_{m-1,n} + U_{m+1,n} + U_{m,n-1} + U_{m,n+1}. \quad (3)$$

Unlike its one-dimensional counterpart, Eq. (3) does not admit an exact analytical solution. A possibility to develop an approximate solution is to use a truncated lattice. The simplest version of the truncation is illustrated

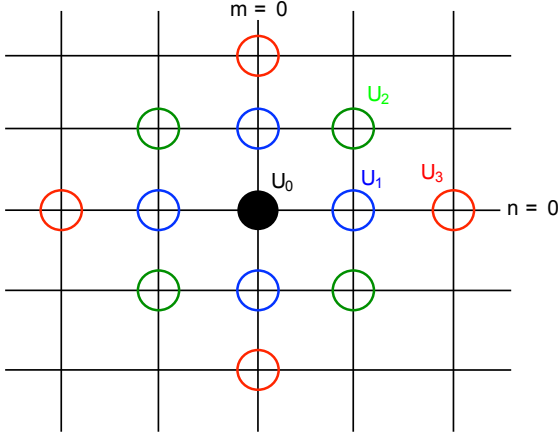


FIG. 1. (Color online) The sketch of the truncated square lattice, which consists of 13 sites. The real amplitude,  $U_0$  (black), and three complex ones,  $U_1$  (blue circles),  $U_2$  (green circles), and  $U_3$  (red circles) are defined here too.

in Fig. 1, where four independent amplitudes are defined:  $U_0$  (at the center),  $U_1$  (in the first rhombic layer surrounding the center), and  $U_{2,3}$  (two independent amplitudes in the second rhombic layer). The amplitudes in all other layers, i.e.  $U_{4,5,\dots}$  are set to zero. At  $(m, n) \neq (0, 0)$ , Eq. (3) is truncated and yield:

$$U_3 = \frac{U_1}{2K}, \quad U_2 = \frac{U_1}{K}, \quad U_1 = \frac{2K}{4K^2 - 5} U_0, \quad (4)$$

where the central amplitude  $U_0$  may be defined to be real, and the complex coefficient is

$$K \equiv 2 + k - i\gamma. \quad (5)$$

The remaining nonlinear equation (1) at  $m = n = 0$  reduces to a single complex equation relating the real intensity  $U_0^2$  and propagation constant  $k$ :

$$\frac{iK(4K^2 - 9)}{4K^2 - 5} - (\Gamma_1 + i\Gamma_2) = (iB - E) U_0^2. \quad (6)$$

One can solve the above equation numerically for the central (peak) amplitude  $U_0$  and propagation constant  $k$ . Consequently the amplitudes in the subsequent layers can be obtained from (4).

The accuracy of the truncated lattice analysis can be improved by including more rhombic layers in the calculations. Although Eqs. (4) and (6) will become more complicated in doing so, they are still easy to solve numerically. Table I shows the numerically obtained  $U_0$  and  $k$  for different truncated lattice models at two different sets of parameters. In any case, convergence is observed by increasing the number of rhombic layers in the analysis.

TABLE I. Numerical solutions for different truncated lattice models at  $B = 1$ ,  $E = 0.1$ ,  $\gamma = 0.5$ , and  $\Gamma_2 = 0.8$ .

	$\Gamma_1 = 0.8574$		$\Gamma_1 = 0.7861$	
Number of rhombic layers	$k$	$U_0$	$k$	$U_0$
2	2.2926	1.8020	1.4005	1.5107
3	2.2870	1.8002	1.3633	1.4962
4	2.2866	1.8000	1.3580	1.4942

#### IV. THE LINEAR-STABILITY ANALYSIS

The stability of the pinned modes was studied by means of the linearization procedure [7]. To this end, perturbed solutions were taken as

$$u_{m,n} = [U_{m,n} + \epsilon V_{m,n}(z)] e^{ikz}, \quad (7)$$

where  $V_{m,n}(z) = X_{m,n}(z) + iY_{m,n}(z)$  is a complex perturbation with an infinitesimal amplitude  $\epsilon \ll 1$ . Substituting this into Eq. (1) results in a linear system that governs the evolutions of the perturbations  $X_{m,n}$  and  $Y_{m,n}$ :

$$\begin{aligned} X'_{m,n} &= \frac{-1}{2} (Y_{m-1,n} + Y_{m+1,n} + Y_{m,n-1} + Y_{m,n+1} - 4Y_{m,n}) \\ &\quad + kY_{m,n} - \gamma X_{m,n} + \delta_{m,0}\delta_{n,0} \{ (\Gamma_1 X_{m,n} - \Gamma_2 Y_{m,n}) \\ &\quad - B [2P_{m,n}Q_{m,n}X_{m,n} + (P_{m,n}^2 + 3Q_{m,n}^2) Y_{m,n}] \\ &\quad - E [(3P_{m,n}^2 + Q_{m,n}^2) X_{m,n} + 2P_{m,n}Q_{m,n}Y_{m,n}] \} \\ Y'_{m,n} &= \frac{1}{2} (X_{m-1,n} + X_{m+1,n} + X_{m,n-1} + X_{m,n+1} - 4X_{m,n}) \\ &\quad - kX_{m,n} - \gamma Y_{m,n} + \delta_{m,0}\delta_{n,0} \{ (\Gamma_2 X_{m,n} + \Gamma_1 Y_{m,n}) \\ &\quad - B [(3P_{m,n}^2 + Q_{m,n}^2) X_{m,n} + 2P_{m,n}Q_{m,n}Y_{m,n}] \\ &\quad - E [2P_{m,n}Q_{m,n}X_{m,n} + (P_{m,n}^2 + 3Q_{m,n}^2) Y_{m,n}] \} \end{aligned} \quad (8)$$

where  $P_{m,n} = \text{Re}(U_{m,n})$  and  $Q_{m,n} = \text{Im}(U_{m,n})$ . An eigenvalue problem is obtained by substituting  $X_{m,n} = \phi_{m,n} \exp(\lambda z)$  and  $Y_{m,n} = \psi_{m,n} \exp(\lambda z)$  into the above linear system. The stationary mode  $u_{m,n}(z)$  is linearly stable if all the eigenvalues  $\lambda$  satisfy  $\text{Re}(\lambda) \leq 0$ , otherwise it is unstable.

The truncated lattice analysis provides an efficient way to trace solution branches, assuming that the stationary mode is radially symmetric about the hotspot. In what follows, this assumption is relaxed in order to allow a more general modal profile. In other words, the modal amplitudes  $U_{m,n}$  are obtained by numerically solving the full system (1) rather than the truncated lattice models. Figure 2 shows a typical stable mode and its eigenvalue spectrum. The stable mode is radially symmetric and is peaked at the location of the hot spot  $m = n = 0$ . The peak amplitude  $U_{0,0}$  and propagation constants are in quantitative agreement to those given in table I, thus justifying the validity of the truncated lattice analysis.

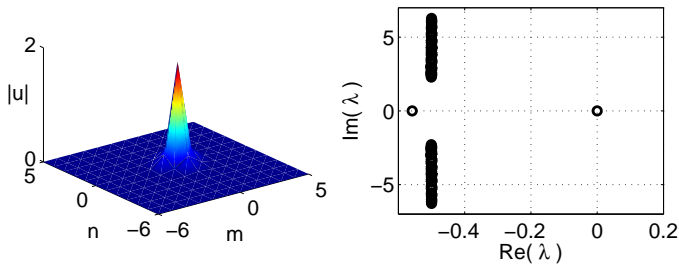


FIG. 2. Top: Stable mode in the form of (2) with peak amplitude  $U_{0,0} = 1.8$  and propagation constant  $k = 2.2865$ . The parameters are  $B = 1$ ,  $E = 0.1$ ,  $\gamma = 0.5$ ,  $\Gamma_1 = 0.8574$ , and  $\Gamma_2 = 0.8$ . Bottom: The eigenvalue spectrum associated with the linearized system (8). All eigenvalues have non-positive real parts.

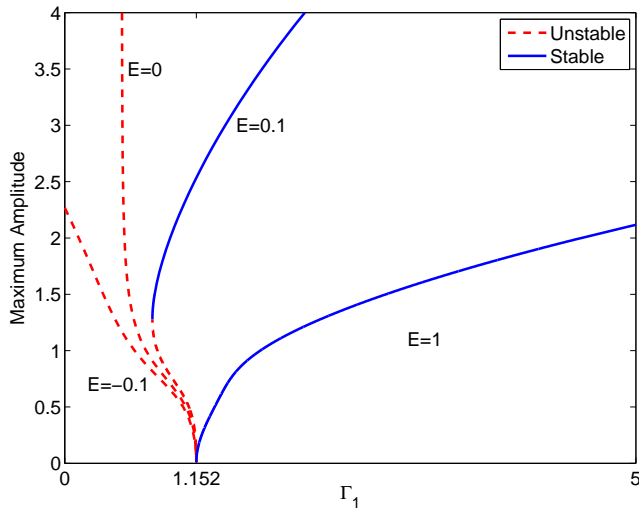


FIG. 3. (Color online) Solution branches for various values of the cubic dissipation  $E$  in the self-focusing regime  $B = 1$ . Stable and unstable branches are denoted by the blue solid lines and red dotted lines, respectively. The rest of the parameters are  $\gamma = 0.5$  and  $\Gamma_2 = 0.8$ .

#### A. Self-Focusing Nonlinearity: $B = +1$

We first studied the stability of pinned modes in the self-focusing regime ( $B = 1$ ). Figure 3 shows the solution branches as functions of the localized linear gain  $\Gamma_1$  at different values of the cubic dissipation  $E$ . Stable solution branches can only be found in the region where  $E > 0$ , i.e. in the presence of cubic loss. For instance, at  $E = 0.1$ , pinned modes with peak amplitudes greater than 1.277 are linearly stable while those with amplitudes less than or equal to 1.277 are all unstable. As mentioned in the previous section, the instability is characterized by the presence of eigenvalues of positive real parts. In any case, the stable and unstable solutions only exist when  $\Gamma_1 \geq 0.7675$  for the parameters consid-

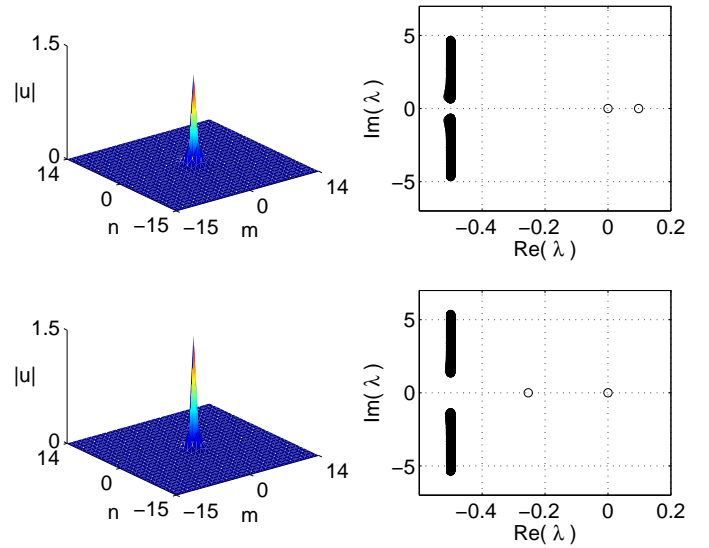


FIG. 4. Top: An unstable pinned mode with a peak amplitude of 1.194 and  $k = 0.6548$  at  $\Gamma_1 = 0.771$  (left) and its eigenvalue spectrum (right). Bottom: A stable pinned mode with a peak amplitude of 1.494 and  $k = 1.3576$  at  $\Gamma_1 = 0.7861$  and its corresponding spectrum. The rest of the parameters are  $B = 1$ ,  $E = 0.1$ ,  $\gamma = 0.5$ , and  $\Gamma_2 = 0.8$ .

ered. When  $\Gamma_1 < 0.7675$ , any initial condition will evolve into the zero solution as there is not enough energy input to support the pulse. Figure 4 shows some typical examples of such stable and unstable solutions. Stability is greatly enhanced by increasing the magnitude of the cubic loss. At  $E = 1$ , all pinned modes are linearly stable, even at very large values of  $\Gamma_1$ . On the other hand, all pinned modes in the absence of cubic dissipation ( $E = 0$ ) or in the presence of cubic gain ( $E < 0$ ) are all unstable. These unstable modes have the same profile as those depicted in Fig. 4 (i.e. radially symmetric and localized at  $m = n = 0$ ) and therefore are not shown here.

Figure 3 shows that all the solution branches emerge from the critical linear gain value  $\Gamma_1 \approx 1.152$ . Moreover, the unstable branch corresponding to  $E = 0$  approaches a vertical asymptote at  $\Gamma_1 = 0.5$  near which the peak amplitude increases drastically. Finally, figure 5 shows the typical evolutions of the unstable modes corresponding to different values of  $E$  obtained from full simulations of Eqs. (1). In the  $E > 0$  case, the cubic loss stabilizes the system, and therefore the unstable mode evolves into the stable mode of the same  $\Gamma_1$  value on the solution branch. However, when  $E \leq 0$  (lack of cubic loss), the unstable modes blow up quickly as there are no stable branches in this regime.

#### B. Self-Defocusing Nonlinearity: $B = -1$

Figure 6 shows the solution branches in the self-defocusing regime  $B = -1$ . In the presence of a small

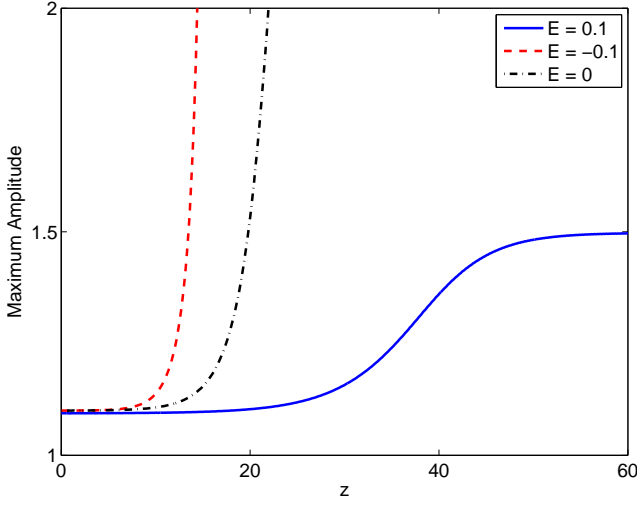


FIG. 5. Evolutions of unstable modes for  $E = 0.1$ ,  $E = -0.1$ , and  $E = 0$ , respectively.  $\Gamma_1$  is chosen such that the initial peak amplitudes are  $|U_{(0,0)}| \approx 1.1$ . The rest of the parameters are  $B = 1$ ,  $\gamma = 0.5$ , and  $\Gamma_2 = 0.8$ .

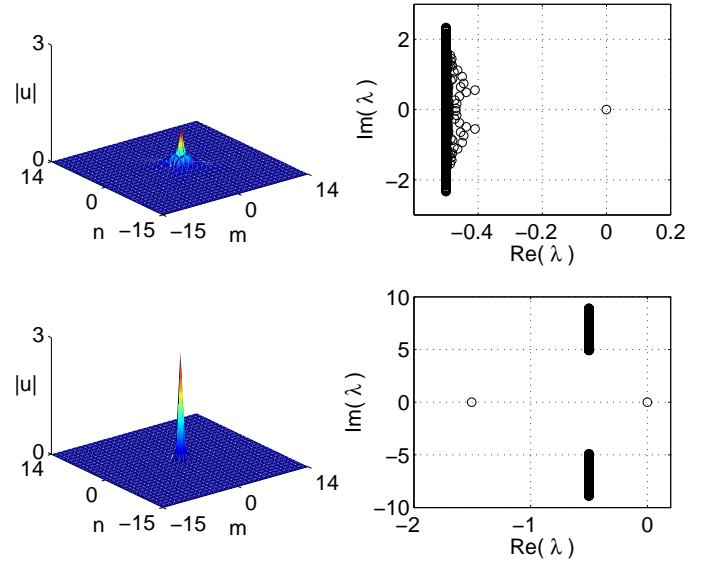


FIG. 7. Bistable solutions with amplitudes of 1.04 (top) and 2.75 (bottom), respectively. Both solutions are obtained with  $\Gamma_1 = 1.268$ ,  $B = -1$ ,  $E = 0.1$ ,  $\gamma = 0.5$ , and  $\Gamma_2 = 0.8$ .

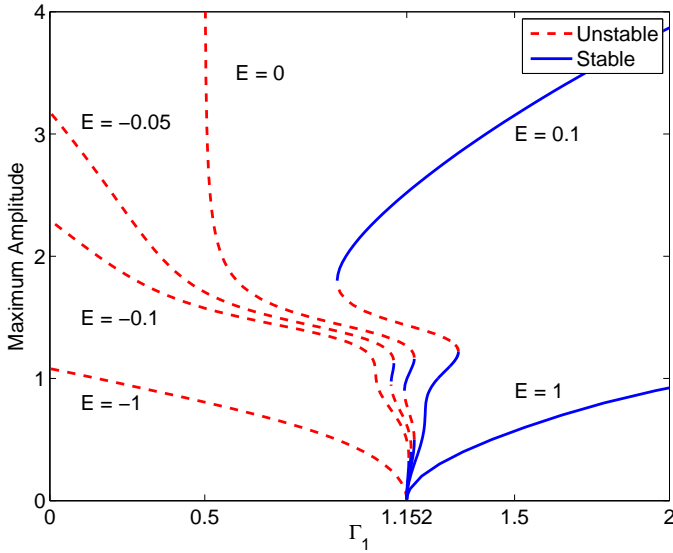


FIG. 6. (Color online) Solution branches for various values of the cubic dissipation  $E$  in the self-defocusing regime  $B = -1$ . Stable and unstable branches are denoted by the blue solid lines and red dotted lines, respectively. The rest of the parameters are  $\gamma = 0.5$  and  $\Gamma_2 = 0.8$ .

cubic loss, the solution branch exhibits a bistability for a certain range of linear gain  $\Gamma_1$ . For instance, at  $E = 0.1$ , stable solutions of different amplitudes co-exist in the region  $1.152 \leq \Gamma_1 \leq 1.319$ . The two stable branches are connected together with an unstable branch whose modal profile and linear spectrum are similar to those found in the self-focusing case (see top panel of Fig. 4) and hence are replicated here. An example of this kind of bistabil-

ity is shown in Fig. 7. The solution with smaller peak amplitude is more spread out. Besides the pulse width, the linear spectra also demonstrate significant difference. When  $E$  increases, the unstable branch is eventually stabilized by the excessive cubic loss and disappears from the bifurcation diagram, and therefore all solutions are stable.

Unlike the self-focusing case, stable solutions are found even in the absence of cubic loss (i.e.  $E \leq 0$ ) in the self-defocusing regime. For small values of cubic gain, bistability similar to those depicted in Fig. 8 is observed. When the magnitude of cubic gain is increased (i.e. making  $E$  more negative), the stable branch with larger peak amplitude disappears. When the cubic gain is too large, all the solutions become unstable. Figure 9 shows the typical evolutions of the unstable modes corresponding to different values of  $E$  obtained from full simulations of Eqs. (1). In the  $E > 0$  case, the initial unstable mode evolves into the “closest” stable mode with the same  $\Gamma_1$  value. Even though a small number of stable modes can be found in the  $E \leq 0$  regime. However, the unstable modes blow up rather than evolve into those stable modes in this regime.

### C. Special Case: $B = 0$

Finally we studied the pulse stability in the special case of  $B = 0$ . Figure 10 shows the stability of different solution branches in this situation. In particular, solutions are always unstable in presence of cubic gain ( $E < 0$ ) and always stable in the presence of cubic loss ( $E > 0$ ). Note that in the case when the cubic dissipation van-

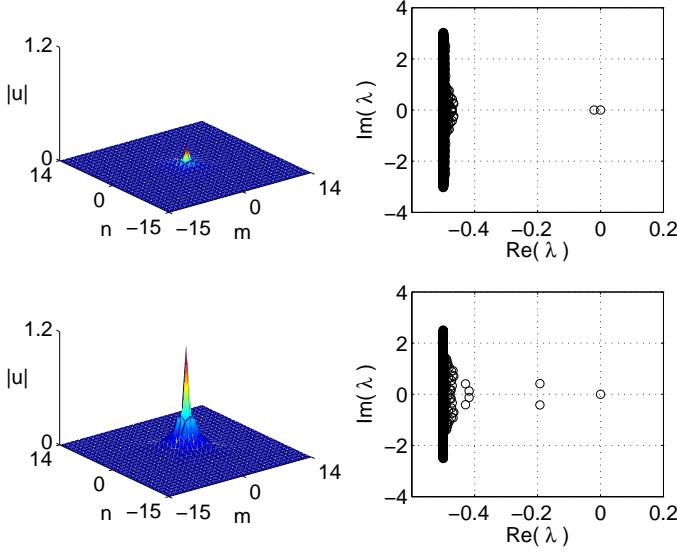


FIG. 8. Bistable solutions with amplitudes of 0.2 (top) and 1.1 (bottom), respectively. Both solutions are obtained with  $\Gamma_1 = 1.159$ ,  $B = -1$ ,  $E = -0.01$ ,  $\gamma = 0.5$ , and  $\Gamma_2 = 0.8$ .

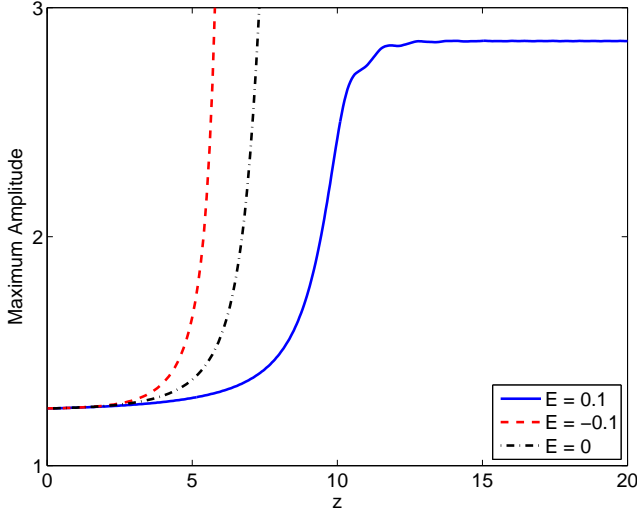


FIG. 9. Evolutions of unstable modes for  $E = 0.1$ ,  $E = -0.1$ , and  $E = 0$ , respectively.  $\Gamma_1$  is chosen such that the initial peak amplitudes are  $|U_{(0,0)}| = 1.25$ . The rest of the parameters are  $B = -1$ ,  $\gamma = 0.5$ , and  $\Gamma_2 = 0.8$ .

ishes, i.e.  $E = 0$ , the governing system (1) admits only one stable solution at a specific gain value ( $\Gamma_1 = 1.152$  with the chosen parameters). Since the system is linear when  $B = E = 0$ , this solution has an arbitrary amplitude which explains why the solution branch is vertical. Figure 11 shows the various stable and unstable solutions and their corresponding linear spectra. Unlike the self-focusing and defocusing regimes, the unstable modes in the  $B = 0$  case evolve into the zero solution rather than

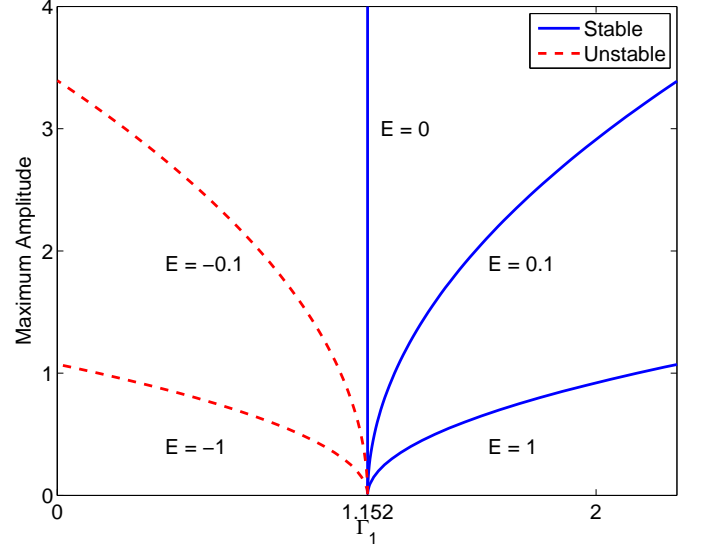


FIG. 10. (Color online) Solution branches for various values of the cubic dissipation  $E$  in the case  $B = 0$ . Stable and unstable branches are denoted by the blue solid lines and red dotted lines, respectively. The rest of the parameters are  $\gamma = 0.5$  and  $\Gamma_2 = 0.8$ .

blow up to infinity.

## V. ONSET OF INSTABILITY OF THE ZERO SOLUTION

In this section we linearize the 2D lattice model (1) by setting  $B = E = 0$  and study the stability of the zero solution around the hot spot. As shown for the one-dimensional continual counterpart of the present work [8], the onset of the local instability of the zero solution, caused by the action of the local gain,  $\Gamma_1 > 0$ , corresponds to the situation when the linearized system generates a solution of the form given by (2) with  $U_{m,n} \neq 0$  everywhere in the lattice.

Unlike the 1D model, an exact analytical treatment is not feasible in the present case due to the complexity of the system. However, the truncated lattice analysis presented in Sec. III provides an efficient way to study the onset of instability in the linearized lattice. In particular, this onset is determined by the critical  $\Gamma_1$  value that makes Eq. (6) solvable (with  $B = E = 0$ ). The  $\Gamma_1$  values found for different truncated models are summarized in table II. As the number of rhombic layers included in the calculations increases, we expect the threshold value of the instability onset to slowly converge to the numerically predicted value  $\Gamma_1 \approx 1.152$  which corresponds to the point for which the solution branches in Figs. 3, 6, and 10 emanate from.



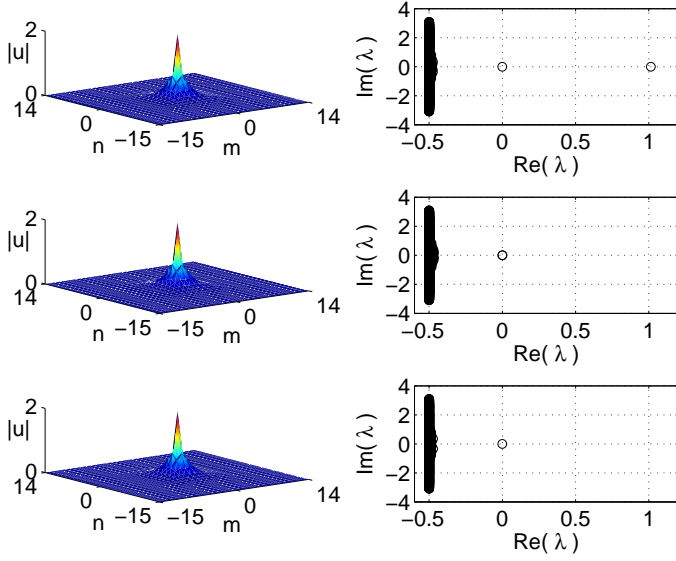


FIG. 11. Solutions with a peak amplitude of 2 at different values of  $\Gamma_1$  and  $E$  (left) and their corresponding spectra (right). Top:  $(\Gamma_1, E) = (0.7521, -0.1)$ . Middle:  $(\Gamma_1, E) = (1.1521, 0)$ . Bottom:  $(\Gamma_1, E) = (1.5521, 0.1)$ . The rest of the parameters are  $B = 0$ ,  $\gamma = 0.5$ , and  $\Gamma_2 = 0.8$ .

TABLE II. Critical  $\Gamma_1$  values for different truncated lattice models  $\gamma = 0.5$  and  $\Gamma_2 = 0.8$ .

Number of rhombic layers	$\Gamma_1$
2	1.4756
3	1.0078
4	1.0955
5	1.1886
6	1.1411

## VI. DUAL HOT SPOTS: SYMMETRIC AND ANTISYMMETRIC MODES

Finally, we briefly studied pinned modes in a lattice with two hot spots. The truncated lattice analysis was first used to obtain simplified equations like Eq. (6) to describe the dual hot spot configuration. For illustration purposes, we assumed the two hot spots were located at  $n = 0$  and  $m = \pm 1$ . Unlike the case of the previous single hot spot configuration, pinned modes in the dual hot spot configuration can be classified as symmetric and antisymmetric. While the amplitudes at the hot spots are taken to be real without the loss of generality, a symmetric mode requires that  $U_{(-1,0)} = U_{(1,0)}$ , and an antisymmetric mode requires that  $U_{(-1,0)} = -U_{(1,0)}$ . The simplest truncated lattices, which only consist of one rhombic layer surrounding the hot spots, are shown in Fig. 12. For the symmetric mode configuration (top panel), a calculation similar to that presented in Sec. III

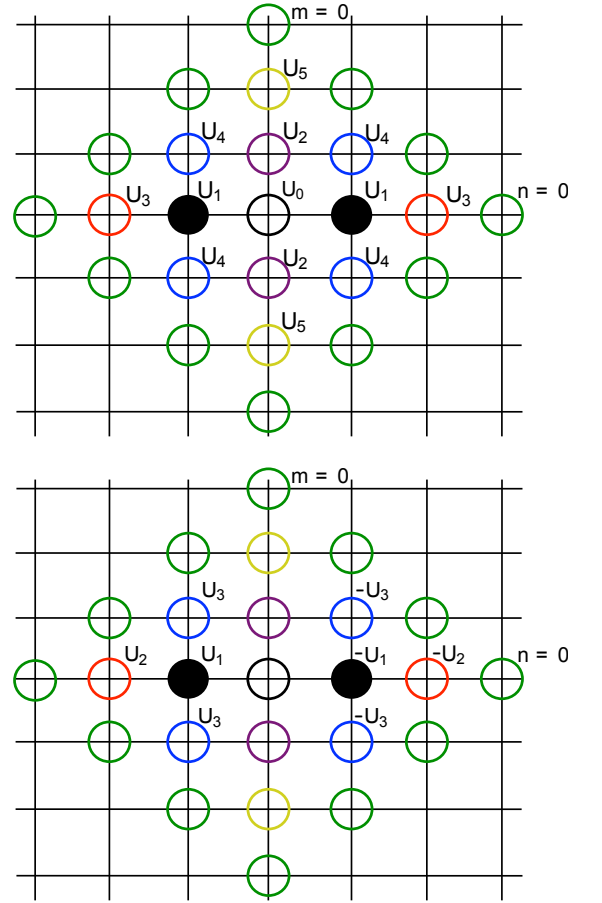


FIG. 12. (Color online) The sketch of the truncated lattice of the dual hot spot configuration with one rhombic layer for the symmetric (top) and antisymmetric modes (bottom). Here  $U_1$  denotes the amplitude (real) at the hot spots. The antisymmetric mode also requires that the amplitudes along the  $m = 0$  locations to be zero. For both models, the amplitudes at the peripheral (green circles) are assumed to be zero.

yields the equation

$$\frac{i(16K^4 - 40K^2 + 9)}{4K(4K^2 - 5)} - (\Gamma_1 + i\Gamma_2) = (iB - E)U_1^2, \quad (9)$$

with  $K$  given by (5), whereas the antisymmetric mode configuration (bottom panel) gives

$$\frac{i(4K^2 - 3)}{4K} - (\Gamma_1 + i\Gamma_2) = (iB - E)U_1^2. \quad (10)$$

More accurate truncated models with more rhombic layers can be derived in the same manner.

Table III gives the numerical values of the propagation constant  $k$  and the hot site amplitude  $U_1$  for both the symmetric and antisymmetric lattices. We compare these results to full numerical simulations of the dual hot site version of Eq. (1). Figure 13 shows that stable pinned modes (either symmetric or antisymmetric), indicated by

TABLE III. Numerical solutions for different truncated lattice models at  $B = 1$ ,  $E = 0.1$ , and  $\gamma = 0.5$ . For the symmetric lattices,  $\Gamma_1 = 1.5445$  and  $\Gamma_2 = -4.2224$ . For the antisymmetric lattices,  $\Gamma_1 = 0.8484$  and  $\Gamma_2 = 0.8$ .

Number of rhombic layers	Symmetric		Antisymmetric	
	$k$	$U_1$	$k$	$U_1$
1	-3.4439	1.8903	2.2535	1.811
2	-3.6721	1.8114	2.2271	1.8009

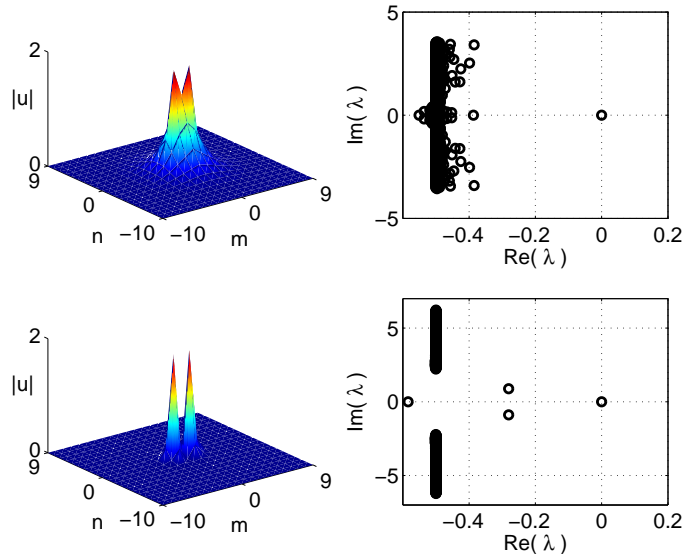


FIG. 13. Top: A stable symmetric mode (left) with peak amplitude of 1.8 and  $k = -3.5445$  at  $\Gamma_1 = 1.5445$  and  $\Gamma_2 = -4.2224$ , and its eigenvalue spectrum (right). Bottom: A stable antisymmetric mode (left) with peak amplitude of 1.8 and  $k = 2.2243$  at  $\Gamma_1 = 0.8484$  and  $\Gamma_2 = 0.8$ , and its eigenvalue spectrum (right). The rest of the parameters are  $B = 1$ ,  $E = 0.1$ , and  $\gamma = 0.5$ . The locations of the hot sites are at  $n = 0$  and  $m = \pm 1$ .

the absence of eigenvalues of positive real parts, can be found in such a configuration. The hot site amplitudes for the symmetric (top) and antisymmetric (bottom) modes are found to be 1.8 and 1.8344, respectively. These are in good agreement with the prediction of the truncated lattice analysis.

## VII. CONCLUSIONS

We have introduced the 2D discrete dynamical system based on the linear lossy lattice into which a single non-linear site with the linear gain (HS, “hot spot”) is embedded. The system can be readily implemented in the form of an array of optical or plasmonic waveguides, admitting selective excitation of individual cores, by the local application of the pump to the uniformly doped cores.

## ACKNOWLEDGMENTS

B. A. Malomed and E. Ding acknowledge the hospitality of the Department of Mechanical Engineering at the University of Hong Kong. Partial financial support was provided by the Hong Kong Research Grants Council contract HKU 711713E.

[1] D. N. Christodoulides and R. I. Joseph, Opt. Lett. **13**, 794 (1988).

[2] N. K. Efremidis and D. N. Christodoulides, Phys. Rev. E **67**, 026606 (2003); K. Maruno, A. Ankiewicz, and N.



- Akhmediev, Opt. Commun. **221**, 199 (2003); Phys. Lett. A **347**, 231 (2005); A. Mohamadou, A. K. Jiotsa, and T. C. Kofane, Phys. Rev. E **72**, 036220 (2005); C. Dai and J. Zhang, Opt. Commun. **263**, 309 (2006); N. K. Efremidis, D. N. Christodoulides, and K. Hizanidis, Phys. Rev. A **76**, 043839 (2007); N. I. Karachalios, H. E. Nistazakis, and A. N. Yannacopoulos, Discr. Cont. Dyn. Syst. **19**, 711 (2007); D. Mihalache, D. Mazilu, and F. Lederer, Eur. Phys. J. Special Topics **173**, 255 (2009); C. Mejia-Cortes, J. M. Soto-Crespo, M. I. Molina, and R. A. Vicencio, Phys. Rev. A **82**, 063818 (2010); C. Mejia-Cortes, J. M. Soto-Crespo, R. A. Vicencio, and M. I. Molina, *ibid.* **83**, 043837 (2011).
- [3] F. Lederer, G. I. Stegeman, D. N. Christodoulides, G. Asanto, M. Segev, and Y. Silberberg, Phys. Rep. **436**, 1 (2008).
- [4] A. Christ, S. G. Tikhodeev, N. A. Gippius, J. Kuhl, and H. Giessen, Phys. Rev. Lett. **91**, 183901 (2003); A. Christ, T. Zentgraf, J. Kuhl, S. G. Tikhodeev, N. A. Gippius, and H. Giessen, Phys. Rev. B **70**, 125113 (2004); Y. S. Bian, Z. Zheng, X. Zhao, Y. L. Su, L. Liu, J. S. Liu, J. S. Zhu, and T. Zhou, IEEE Phot. Tech. Lett. **24**, 1279 (2012).
- [5] E. Kenig, B. A. Malomed, M. C. Cross, and R. Lifshitz, Phys. Rev. E **80**, 046202 (2009).
- [6] B. A. Malomed, E. Ding, K. W. Chow and S. K. Lai, Phys. Rev. E **86**, 036608 (2012).
- [7] E. D. Farnum and J. N. Kutz, J. Opt. Soc. Am. B **25**, 1002 (2008).
- [8] C. K. Lam, B. A. Malomed, K. W. Chow, and P. K. A. Wai, Eur. Phys. J. Special Topics **173**, 233 (2009).